Recent Advances in Higher-Order, Multimodal, Biomedical Imaging Agents

*James Rieffel, Upendra Chitgupi, and Jonathan F. Lovell**

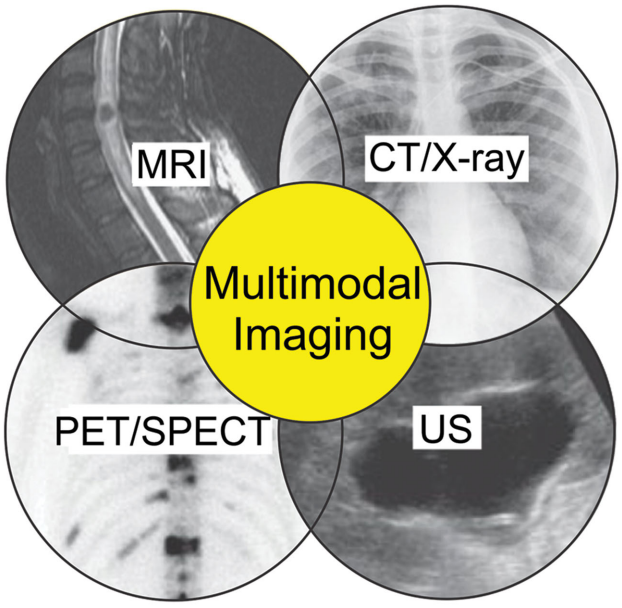

From the Contents

***A**dvances in biomedical imaging have spurred the development of integrated multimodal scanners, usually capable of two simultaneous imaging modes. The long-term vision of higher-order multimodality is to improve diagnostics or guidance through the analysis of complementary, data-rich, co-registered images. Synergies achieved through combined modalities could enable researchers to better track diverse physiological and structural events, analyze biodistribution and treatment efficacy, and compare established and emerging modalities. Higher-order multimodal approaches stand to benefit from molecular imaging probes and, in recent years, contrast agents that have hypermodal characteristics have increasingly been reported in preclinical studies. Given the chemical requirements for contrast agents representing various modalities to be integrated into a single entity, the higher-order multimodal agents reported so far tend to be of nanoparticulate form. To date, the majority of reported nanoparticles have included components that are active for magnetic resonance. Herein, recent progress in higher-order multimodal imaging agents is reviewed, spanning a range of material and structural classes, and demonstrating utility in three (or more) imaging modalities.*

DOI: 10.1002/smll.201500735

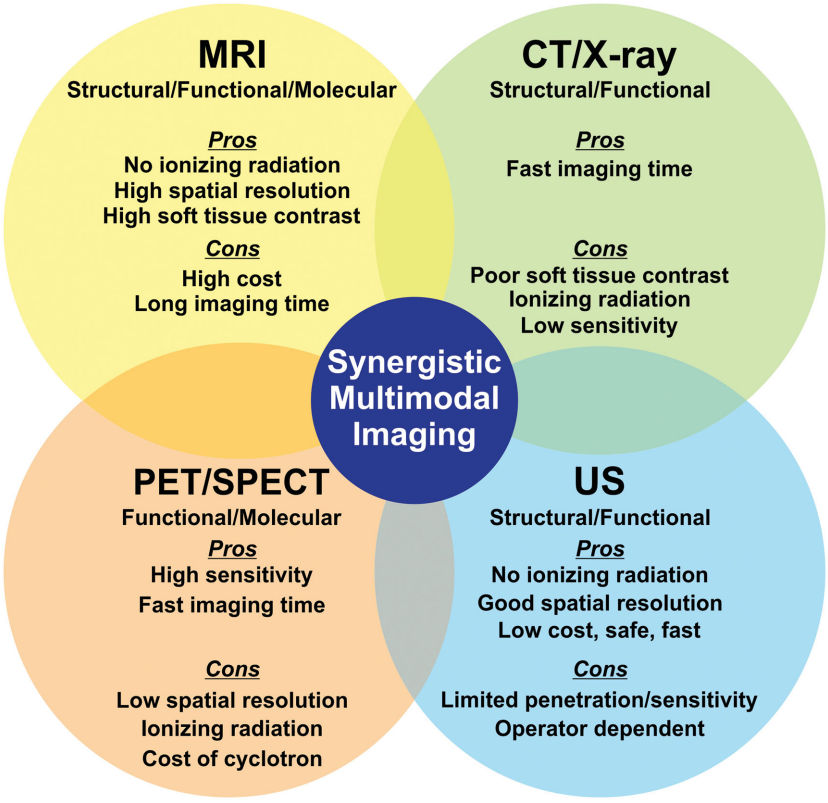

Figure 1. Overview of common clinical imaging modalities which have potential for multimodal applications. MRI: magnetic resonance imaging, CT: computed tomography, PET: positron emission tomography, SPECT: single-photon emission tomography, US: ultrasound.

1. Introduction

Medical imaging is an interdisciplinary field that commands a significant proportion of all medical-related spending costs. Despite the indispensable benefits that clinical medical imaging modalities offer, X-ray computed tomography (CT), magnetic resonance imaging (MRI), ultrasound (US), positron emission tomography (PET), single-photon emission computed tomography (SPECT), and their derivatives, all have characteristic strengths and drawbacks.[1,2] A cursory overview of the characteristics of these clinical imaging modalities is presented in **Figure 1**. Whether it is a high cost, low resolution, exposure to ionizing radiation, poor sensitivity to contrast media, or difficulty in data interpretation, emerging imaging paradigms and technologies strive to address unmet needs.[3] One direction this has taken is towards multimodality in medical imaging.

Multimodal imaging can be any combination of techniques resulting in a composite image from separate sources. In theory, by combining two or more methods, one can overcome the limitations of each modality independently. Ideally, this results in obtaining higher-quality or more useful data than could be achieved otherwise. Higher-order multimodal imaging extends this concept to a greater number of imaging modalities and implies that interconnected modality synergies are exploited for the purpose of generating complementary and informative insights. In a typical example, Kircher et al. demonstrated this powerful paradigm by designing and testing an MRI/photoacoustic (PA)/surface-enhanced Raman scattering (SERS) contrast agent to aid in brain tumor margin delineation and resection. Overcoming the sensitivity, specificity, and resolution limitations of each modality by itself, researchers were able to use a probe for pre- and intra-operative surgical planning, as well as to identify cancerous tumor margins (**Figure 2**).[4] This synergistic imaging takes advantage of the strengths of each of the different imaging modes, which is at the core of what multimodality has to offer.

The rapid increase in academic research involving multimodal imaging is shown in **Figure 3**. The increased output in multimodal agents at the research stage is likely to be followed by the development and commercialization of some of these recent advances. Several comprehensive reviews of multimodal contrast agents have been reported in recent years,[5–9] which discuss the many classes of nanoparticles and their various therapeutic and diagnostic qualities. In this review, we describe recent examples of higher-order imaging probes, most of which are trimodal, but some of which go beyond.

2. Overview of Medical Imaging

Medical imaging techniques can be generally classified as either yielding structural or functional information. Structural imaging looks primarily at the size, shape, and morphology of objects in the body. This type of imaging can target bones, organs, and vessels and looks for physical or anatomical abnormalities in the structure and can guide medical procedures. Functional imaging looks at the physiology of diverse and dynamic bioprocess at the cellular or whole-organ level and is often associated with molecular imaging. This imaging has been used in visualizing metabolism in different tissues, blood flow, detecting molecular targets, and diffusion/perfusion/biodistribution. Both structural and functional imaging modalities are important in everyday clinical applications and preclinical experiments.

J. Rieffel, U. Chitgupi, Prof. J. F. Lovell
Department of Biomedical Engineering
University at Buffalo
State University of New York
Buffalo, NY, USA
E-mail: jflovell@buffalo.edu

DOI: 10.1002/smll.201500735

2.1. Clinical Modalities

Computed tomography (CT) is the result of emitting and detecting X-rays from multiple angles around an object in order to elucidate internal structures. Although it relies on ionizing radiation, CT is considered the gold standard for identifying structural abnormalities such as tumors, hemorrhages, bone trauma, vascular and heart disease, emphysema, fibrosis, and more. It is often used in diagnosing conditions including those of the head, chest, abdomen, pelvis, heart, and the upper gastrointestinal (GI) tract.[10] While CT has had a transformative impact on medicine, due to the risks induced by the ionizing radiation on which it relies, there has been concern about the risk posed to children and by unnecessary scans.[11]

Magnetic resonance imaging (MRI) is more expensive than CT but does not involve ionizing radiation and is especially useful for visualizing soft tissues.[12] Like CT, MRI also plays a large role in both clinical and preclinical imaging. Although its cost generally keeps it from screening applications, the benefits and potential of MRI diagnosis and treatment planning are accepted. There are many variations of MRI that can provide both structural and functional information.

Ultrasound or ultrasonography (US) is one of the most commonly used types of medical imaging because it is affordable, widely accessible, transportable, real-time, and is free of ionizing radiation. Utilizing acoustic vibrations with a frequency greater than the human range of hearing, and translating the effects of tissue on these waves, forms the foundation of diagnostic sonography. It has many clinical and preclinical research applications in prenatal medicine and in diagnosis of diseases in most the major organs, with variations like Doppler echocardiography and elastography capable of discerning both structural and functional features. Drawbacks to US technology include large amounts of noise and a limited ability to penetrate deep into tissue, where resolution falls with depth. There has been work to develop endocavity transducers to image internal structures at higher frequencies and resolutions.

Positron emission tomography (PET) and single-photon emission computed tomography (SPECT) are primarily tracer imaging techniques, which require the introduction of exogenous agents. These two molecular imaging modalities rely on the decay of radionuclides, usually incorporated into a bioactive molecule such as glucose. These analogues can be traced once administered into the body for minutes or hours and provide information about the activity of biological processes. The most commonly performed PET scans use this strategy to identify areas in the body exhibiting abnormally high levels of sugar metabolism, as an indication of tumor growth, for example.[13] Although their oncologic applications are the most common, PET and SPECT are also used for imaging neural activity, myocardial function, and drug distribution.

2.2. Emerging and Preclinical Modalities

Although emerging imaging modalities, by definition, have yet to experience the same clinical success as those just described (CT, MRI, US, PET), technologies like photoacoustic imaging (PA), Raman imaging, and upconversion luminescence (UCL) imaging hold the potential for contributions in the field. There are many variations on these modalities and the ways they can be implemented.

Optical and fluorescence microscopy have been used in medicine for decades as ex vivo or in vitro tools, often for examining histological tissue samples or living cells. This is because visible light has poor tissue penetration and experiences significant scattering in biological media. Recently there has been an increase in the work done to create systems for optical and fluorescence imaging of the whole body that can be performed on a subject without any need for complicated biopsy and staining protocols.[14] Optical techniques that can complement or replace conventional modalities are desirable because visible light radiation causes no harmful ionizing effects to the patient, and the cost of materials is cheaper compared to other highly sensitive techniques like PET and SPECT. One benefit to optical imaging is its ability to be

James Rieffel is a MSc candidate in the Biomedical Engineering Department at the State University of New York at Buffalo. James is from Ithaca, NY, and received his BS in biology from SUNY Geneseo with a minor in biomathematics. James is interested in the characterization and functionalization of emerging multimodal nanoscale imaging agents for biomedical applications

Upendra Chitgupi is pursuing his MSc in Biomedical Engineering at the State University of New York at Buffalo. He previously completed his undergraduate degree at the B. M. S. College of Engineering in Bangalore, India. His research involves developing new nanoparticles for imaging and therapy.

Jonathan Lovell is an assistant professor of biomedical engineering at the State University of New York at Buffalo. He received his PhD in biomedical engineering from the University of Toronto following an MSc in biochemistry at McMaster University and an undergraduate degree in Systems Design Engineering at University of Waterloo. His main interests involve the development of translatable nanoplatforms for better diagnosis and combatting disease.

DOI: 10.1002/smll.201500735

www.MaterialsViews.com

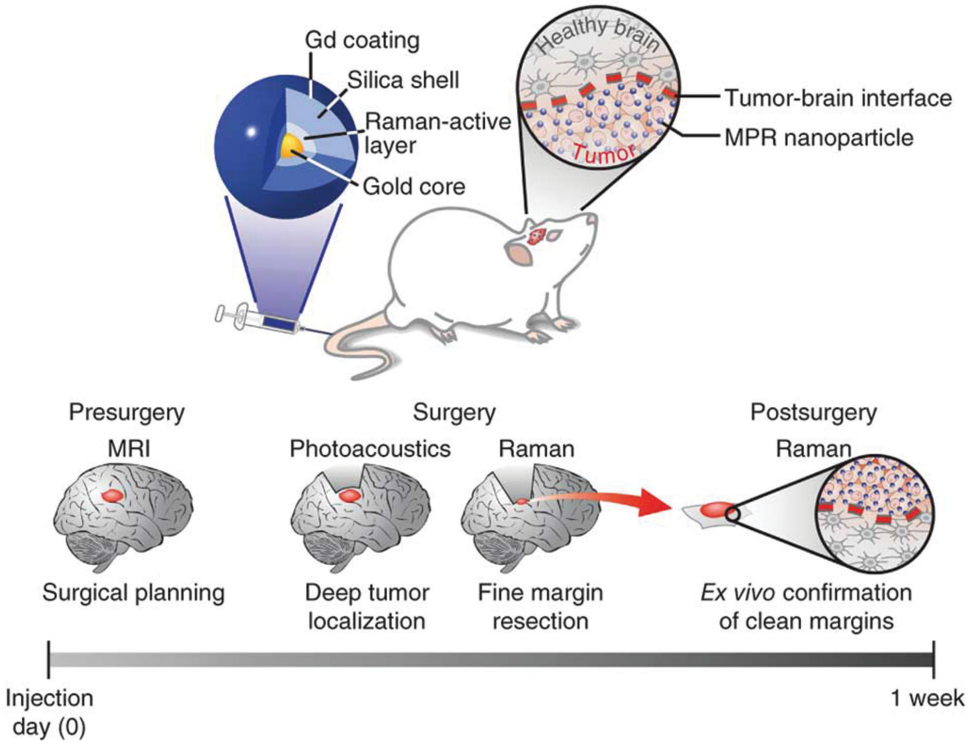

Figure 2. Synergistic use of a triple-modality MR/Raman/PA probe (MPR). MPRs are injected intravenously into a mouse bearing an orthotopic brain tumor and accumulate in the tumor (top). The concept of proposed eventual clinical use (bottom). Detectability of MPRs by MR allows preoperative detection and surgical planning. The probe can be detected in the tumor during surgery several days later. PA, with its relatively high resolution and deep tissue penetration, is then able to guide bulk tumor resection intraoperatively. Raman imaging, with its ultrahigh sensitivity and spatial resolution, can then be used to remove any residual microscopic tumor burden. The resected specimen can subsequently be examined using a Raman probe ex vivo to verify clear tumor margins. Adapted with permission.[4] Copyright 2012, Nature Publishing Group.

miniaturized to the level of a catheter or endoscope. Endoscopic imaging uses flexible tubes combined with light sources and a camera, which can be inserted into the body with minimal invasiveness. With white light as the illumination source, surgeons have been able to see inside many parts of the body without large surgical incisions and perform many essential procedures in this way. Recently, there have been significant advances in miniaturizing the hardware necessary for confocal and fluorescence imaging to the point that there are multiple commercially available confocal endomicroscope probes available. It has been shown, for example, that through using fluorescent antibodies as probes, not just the presence but also the variants of human bladder cancer can be identified.[15]

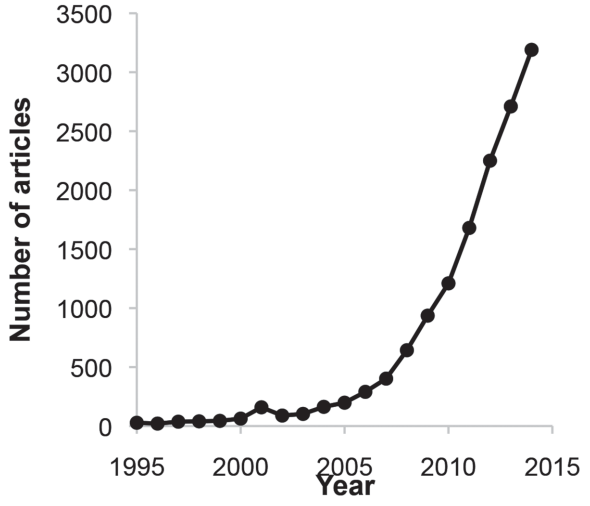

Figure 3. Growth of multimodal imaging research. The number of articles published per year containing the term "multimodal imaging" between 1995 and 2014 in the Google Scholar database.

Photoacoustic tomography (PAT) is an exciting, emerging imaging modality. Based on the photoacoustic effect, this technique relies on the absorption of photons by endogenous biomolecules or exogenous contrast agents that then generate ultrasonic waves, which experience less scattering compared to light waves in tissue. With the ability to image a wide scale of sizes from organelles to organs and with no use of ionizing radiation, it is not surprising this modality is trying to establish a clinical niche in breast cancer imaging, mapping sentinel lymph nodes, and brain imaging.[16] It has been used for the functional imaging of blood flow as well as yielding structural information from the cellular level up through whole-organ imaging. Because of its strength and versatility, there has been work on the miniaturization of PA systems for endoscopic integration.

Raman spectroscopy is an optical technique that can be used to identify chemicals in a manner similar to infrared spectroscopy. Using physical and chemical properties on the molecular scale, Raman spectroscopy is especially powerful in distinguishing subtle differences in tissue composition or

DOI: 10.1002/smll.201500735

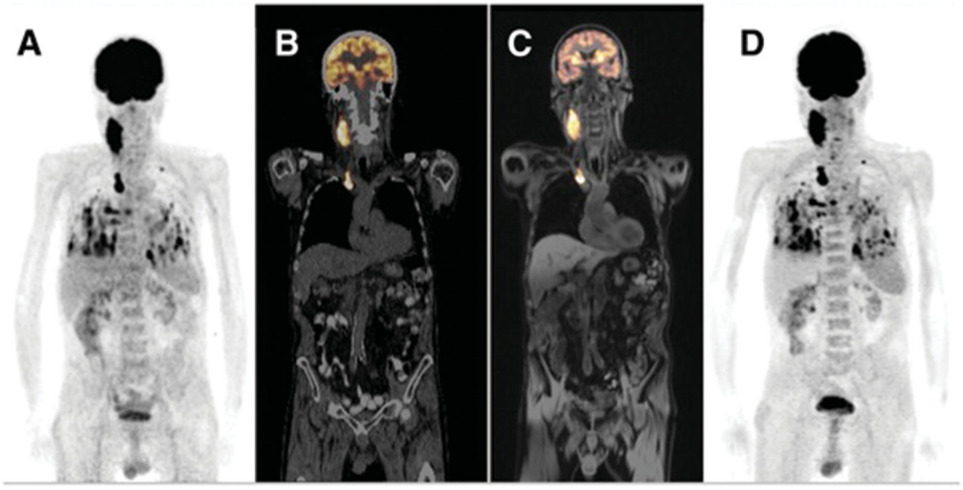

Figure 4. Similarity of PET/CT and PET/MRI scans, acquired on the same day in the same patient with metastasized thyroid carcinoma. A) ^{18}F-FDG PET acquired on PET/CT scanner. B) Overlay of PET (in orange) and structural low-dose CT data acquired on a PET/CT scanner. C) Overlay of PET (in orange) and MRI acquired on PET/MR scanner. D) ^{18}F-FDG PET acquired on PET/MR scanner. An overall similarity can be seen in pattern of suspicious lesions in (A) and (D). Adapted with permission.[78] Copyright 2012, Society of Nuclear Medicine and Molecular Imaging.

the conformational structure of pharmaceuticals and nanoparticles. In the design of biological probes, it is often desirable to track multiple targets simultaneously. To this effect, nanoparticles designed with a surface-enhanced Raman scattering (SERS) functionality have been synthesized with differences in their chemical structure (vibrational modes) that allow the highly multiplexed interrogation of biological systems.[17]

3. Higher-Order Multimodal Imaging

Developments in image acquisition and reconstruction in each independent modality have enabled the field of multimodal imaging to expand. This originally came about by using two modalities in tandem, one right after the other, but has evolved into commercial production of integrated clinical PET/CT and PET/MRI machines, and preclinical small-animal imaging machines capable of many combinations of modalities. The IVIS Lumina XRMS is a single scanner manufactured by PerkinElmer capable of X-ray, FL, and Cerenkov imaging. The development of these integrated scanners has stimulated a further increase of multimodal contrast agents with diverse applications.

The first clinical implementation of multimodal imaging was combined PET–CT.[18] The strength of this combination comes from being able obtain a greatly increased amount of information regarding structure (CT) as well as physiological function (PET) that provides information that would be unattainable with standalone modalities. This technology has virtually replaced standalone PET scanners and gained clinical acceptance at an unprecedented rate so that the clinical benefit of PET–CT over PET alone has been established.[19] Although combined PET–MRI scanners began development around the same time as PET–CT, cost and technical challenges have delayed the widespread embracement of those machines.[6] **Figure 4** demonstrates the similarity between images acquired with PET–CT and PET–MRI.

The main challenges with the clinical implementation of multimodal imaging are that, with the high demands on effective communication of all parties involved, unique protocols have to be developed in each clinical setting. Making sure that all scans are performed correctly, the digital formats are appropriate, and that qualified people perform the analysis, is a highly demanding task. Then there are also technological drawbacks that are difficult to overcome without integrated scanners, such as issues from patients breathing or registering kinetics of a disease or treatment. Combined PET–CT scanners have taken tremendous steps in overcoming these challenges, but are still in active stages of improvement.

While PET–CT and PET–MRI have already been developed and implemented clinically, there are many other combined imaging techniques being explored for synergistic benefits. It is most common to see a combination of one of the more established anatomical modalities such as CT or MRI used in conjunction with more novel functional techniques like PA or UCL. Many bimodal imaging probes have been developed, encompassing virtually any combination of modalities, often with additional targeting or therapeutic applications. Although there are preclinical scanners available from different manufacturers that can combine CT or PET with FL for in-vivo imaging, often multimodal imaging that incorporates emerging techniques requires scanner modification, imaging in sequence, or building new instrumentation from scratch.

4. Development of Higher-Order Multimodal Contrast Agents

The development of nanoparticle (NP)-based contrast agents capable of multiple modalities has proceeded tremendously in the past decade. Administration of a single, higher-order, multimodal contrast agent presents some pragmatic advantages over multiple separate administrations of different unimodal agents. Having the imaging contrast originating

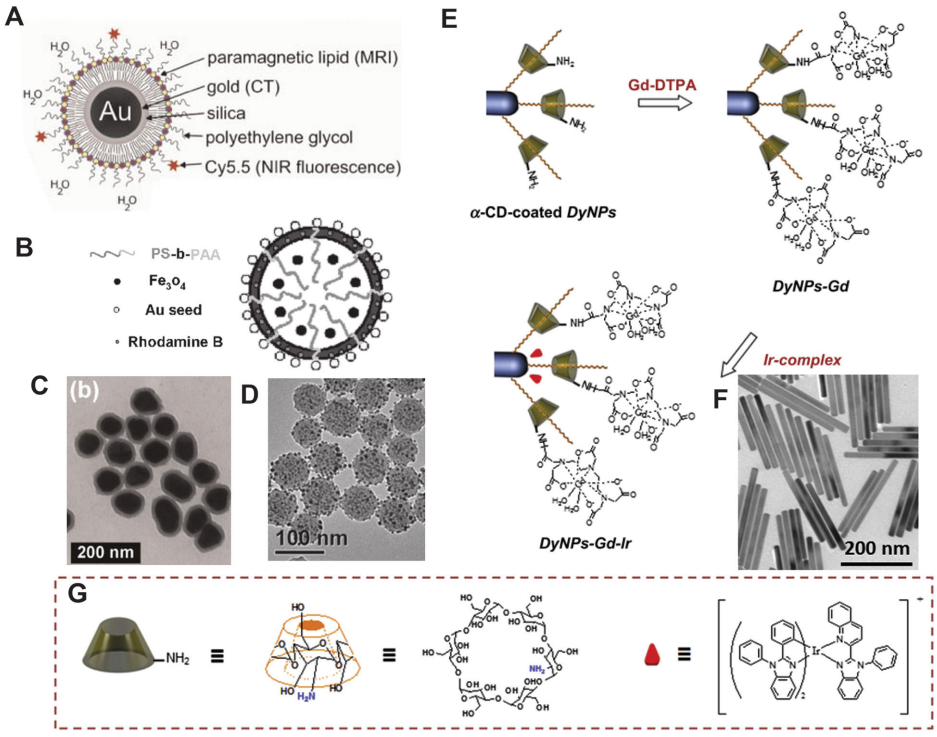

Figure 5. Exemplary NPs used for CT/MRI/FL. Schematic representations of trimodal A) gold/silica core NP (reproduced with permission[27]) and B) Fe_3O_4@dye–hybrid@Au ((reproduced with permission).[28] TEM images of C) gold/silica core NPs and D) Fe_3O_4@dye–hybrid@Au.[28] E) Schematic, F) TEM, and G) molecular structure of alpha-CD and Ir-complex in α-CD-coated DyNP–Gd–Ir.[30] Copyright 2014, Elsevier.

from a single agent also is advantageous. However, unimodal agents for various imaging modalities are already optimized and clinically established, so there is a burden for new multimodal agents to show synergistic superiority over separate unimodal agents. But chemical design and synthesis of NPs capable of multimodality is not simple. Additionally, there could be the possibility of interference in function or storage stability between the various contrast components of integrated multimodal agents.

It may appear at first glance that a trimodal imaging probe that can simultaneously generate contrast in MRI, PET, and FL might be redundant. Although PET and FL probes both have a high sensitivity and can be used to image functional characteristics, there still is reason to combine them into a single integrated probe. Besides differences in the modalities themselves, an important benefit is being able to directly compare imaging metrics like resolution, tissue penetration, and sensitivity without introducing additional confounding factors into the system. When the anatomical resolving power of MRI is incorporated to further analyze these particles in vivo and in vitro, this synergy allows rigorous contrast agent evaluation. Many materials are compatible with higher-order imaging multimodality by incorporating additional functional moieties. For example, some platforms that are suited for multimodal imaging include upconverting NPs,[20,21] quantum dots,[22] iron oxide NPs,[23] silica NPs,[24] liposomes,[25] and lipoproteins.[26] The following examples of multimodal agents are categorized by combined imaging modalities and serve to highlight some representative recent examples.

4.1. CT/MRI/FL

The combination of CT, MRI, and FL is one of the most explored trimodal schemes in multimodal imaging. Both CT and MRI are essential in clinical diagnostics, and FL offers a highly sensitive element capable of detecting and reporting phenomena that may not be possible with the other two. Although MRI and CT can provide similar structural information in many cases, the subtle differences between the implementation, cost, safety, and target tissue to be imaged could determine which imaging technique is most appropriate. FL could then be used in a variety of ways to validate, correlate, or add new information to the observations of the other modalities at low cost and possibly on a cellular or molecular level.

Many materials have been used to impart CT, MRI, and FL imaging capabilities. **Figure 5** shows some representative materials, structural schematics, and transmission electron microscopy (TEM) images of gold/silica core NPs,[27] Fe_3O_4@dye–hybrid@Au NPs,[28,29] and alpha-cyclodextrin (α-CD)-coated nanophosphors (DyNP–Gd–Ir).[30] Finding biocompatible materials that retain their respective magnetic or optical properties without compromising the functionality of the other components is a major challenge in designing multimodal imaging probes. For the gold/silica core particles, the dense core provides contrast for CT, a Gd-chelating lipid is used for MRI, a lipid-conjugated Cy5.5 provides contrast for FL, and polyethyleneglycol distearoylphosphatidylethanolamine (PEG–DSPE) is used to increase biostability (Figure 5A,C).[27] This type of core-coating structure, with

DOI: 10.1002/smll.201500735

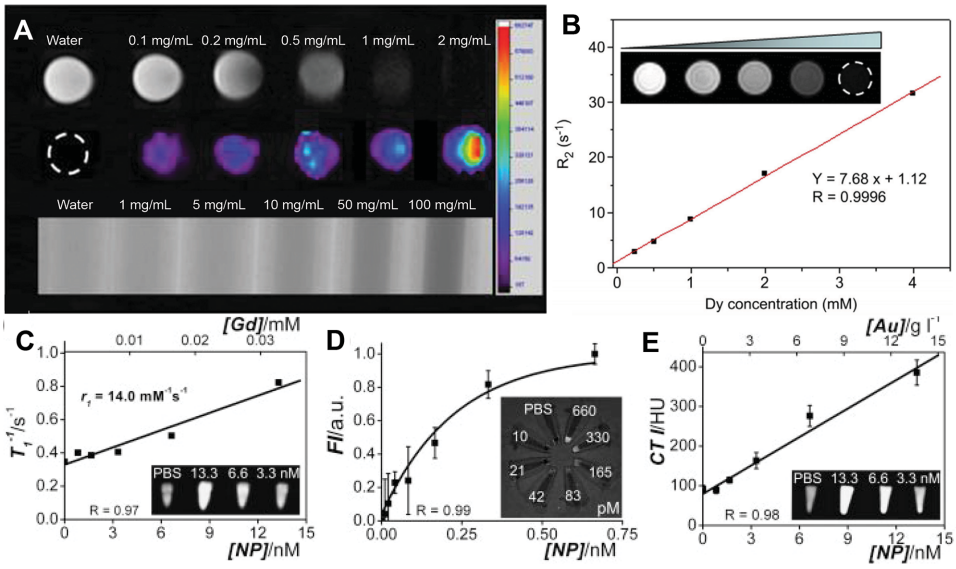

Figure 6. CT/MRI/FL/ imaging in phantoms. A) T2 weighted CT/MRI/FL/ imaging (top to bottom) of phantom i-fmSiO$_4$@SPION samples in aqueous suspension. Reproduced with permission.[31] Copyright 2014, Dovepress. B) R_2 as a function of concentrations of Dy from DyNP–Gd–Ir. Inset: T2-weighted MR images of DyNPsGd-Ir. Reproduced with permission.[30] Copyright 2014, Elsevier. Concentration dependence of gold/silica core NPs for signal generation in C) MRI, D) FL, and E) CT. Reproduced with permission.[27]

active lipid or polymer ligands to impart additional imaging functionality, is a common design. Besides generating enhanced X-ray contrast by employing gold as the core nanoparticle, Au nanospheres have been used to decorate the surface of polymer-based NPs (Figure 5B,D), iodinated oil has been loaded into silicon NPs,[31] and $NaDyF_4$ nanorods were conjugated to polymeric NPs.[30] Polymers like α-CD have been used to chelate Gd (Figure 5E–G), which were shown to enhance both T1- and T2-weighted MRI.[30] Iron oxide (IO) nanoparticles as the core and decorated onto the surface of other NPs have also contributed to MRI contrast in trimodal imaging probes.

Just like there are many components that can be used to generate a trimodal signal in combined CT, MRI, and FL, there are many synthetic methods used to formulate these trimodal probes. The best methods are ones that minimize cost, risk, and time, while having the highest yield, reproducibility, and simplicity. A simple one-pot synthesis was described, where self-assembled amphiphilic polystyrene-*b*-poly(acrylic acid) with hydrophobic Fe_3O_4 nanoparticles were conjugated to Rhodamine B dye and gold nanoparticles were placed on the surface of the core.[28] Since many of the trimodal probes currently being developed also have therapeutic or active targeting properties, the ability to load drugs or to be modified with additional targeting ligands can be useful. A trifunctional imaging probe with superparamagnetic iron oxide nanoparticles (SPIONs) as the core was designed for the additional loading of materials.[31] After functionalization with silicon, Cy5 dye, and PEG for stability, the particles were loaded with iodinated oil to yield trimodal i-fmSiO4@SPIONs.

Phantom studies are ubiquitously performed to test the relationship between signal strength and probe concentration. This can be done in microwell plates or plastic tubes and is one of the more common ways of comparing the performance of new contrast agents to those already in use. Phantom analysis of Fe_3O_4@dye–hybrid@Au in MRI yielded an improved r_2 value more than twice that of commercial iron oxide particles such as Ferridex.[28] With an Au concentration of 146 mg mL^{-1}, the Fe_3O_4@dye–hybrid@Au showed an equivalent contrast enhancement as 160 mg mL^{-1} to the commercial μCT agent eXIA 160. The results obtained by phantom studies sometimes can alternatively be validated or acquired while incubating samples in biological media or in vitro. Phantom i-fmSiO$_4$@SPION and samples in aqueous suspension were imaged as shown in **Figure 6**A.[31] Figure 6B shows that, during incubation with HeLa cells, DyNP–Gd–Ir NPs were able to retain phosphorescence without any photobleaching and showed a direct relation of signal intensity with the concentration of nanoparticles.[30] Figure 6C–E shows the effect of gold/silicon core NP concentrations on MRI, FL, and CT in phantoms.[27] With the rise of endoscopic and real-time imaging-aided surgery, in-vitro and ex-vivo techniques can also help determine the ability of imaging agents to be internalized by cells or label-specific tissues. In this manner, PEGylated Fe_3O_4@dye–hybrid@Au NPs were confirmed to be internalized by normal cells by confocal microscopy, showing no toxicity.[28]

PEGylated Fe_3O_4@dye–hybrid@Au NPs were also evaluated in mice with diethlynitrosamine-induced hepatocellular carcinoma. Following intravenous injection, these NPs helped to differentiate liver lesions from normal tissue.[28] When gold/silica core NPs were administered systemically, enhanced contrast of the abdomen was achieved in MRI and CT.[27] In contrast, 100 μL of DyNP–Gd–Ir NPs were injected at 3 mg mL^{-1} intratumorally. For these NPs, there was an increase in CT contrast, improving 100% from 109 to 212 Hounsfield units. MRI negative contrast and positive contrast in the region of the tumor was found to be 104% and 152% respectively, whereas the change in the surrounding

DOI: 10.1002/smll.201500735

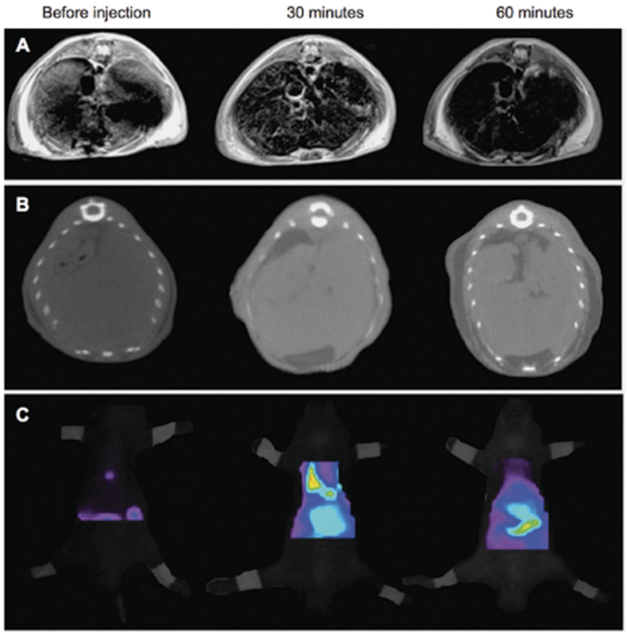

Figure 7. CT/MR/FL images of mouse livers after intravenous injection of i-fmSiO_4@SPIONs at indicated times post-injection. A) T2-weighted MRI, B) CT, and C) FL images. Adapted with permission.[31] Copyright 2014, Dovepress.

tissue was negligible.[30] Even without a cancer model, in vivo tests are essential in comparing imaging metrics between modalities, elucidating biodistribution, and pharmacokinetics. Iodinated oil-loaded i-fmSiO_4@SPIONs were detected, post intravenous injection, in the liver by CT, MRI, and FL, as shown in **Figure 7**.[31]

4.2. CT/MRI/UCL

Although the combination of CT, MRI, and UCL is similar to that of CT, MRI, and FL described above, the substitution of UCL for traditional FL distinguishes this combination with more emphasis on deeper optical imaging in preclinical research and development. Since the depth-dependent limitations of optical imaging have prevented its implementation in deeper tissue with respect to in-vivo imaging applications, the use of UCL has been an important step in overcoming this hurdle. By directly comparing the results of UCL-based optical techniques with CT and MRI, important comparative analysis can be used to push the limits of optical biomedical imaging.

UCNPs have generated recent interest for multimodal imaging and combined therapeutics. Using slightly different synthesis and formulation techniques, researchers can impart CT, MRI, and UCL functionalities.[32–41] UCNP@SiO_2–GdDTPA,[33] upconversion sesame balls (UCS-balls),[35] and multishell, multifunctional nanoprobes (MUCNPs)[36] have been described for this application. UCNP@SiO_2–GdDTPA nanoparticles, which incorporate Gd into a coating polymer, were recently explored.[33,42] In another system, NaY/GdF_4:Yb, Er, Tm nanocrystals were used as the core, coated with silica, and further functionalized with gold nanoparticles through adsorption. Polyethylene glycol was used to obtain biocompatible UCS-balls.[35] Oleic acid-capped $NaYF_4$:Yb/Tm was used as the core material for MUCNPs. An epitaxial coating method sequentially added a thick layer of $NaLuF_4$, a layer of $NaYF_4$, and a layer of $NaGdF_4$ followed for all the shells. Oleic acid was replaced by polyacrylic acid (PAA) and folic acid (FA) to study the performance of MUCNPs as contrast agents and tumor targeting nanoparticles.[36]

Zhou et al. designed a mesoporous core/shell UCNP (mUCNP) with a $NaYbF_4$:2%Er core and a mesoporous $NaGdF_4$ shell without using silicon.[37,43] **Figure 8** illustrates the materials, synthesis schematic, and in-vitro applications of mUCNPs. Other trimodal $BaGdF_5$-based UCNP contrast agents, with a convenient one-pot synthesis[41] and which serve as drug carriers,[32,44] have also been described. For one drug carrier, $BaGdF_5$-based UCNPs, an active shell coating was added and doxorubicin was covalently conjugated.[32] The other drug carrier utilized a two-drug loading scheme to enhance the synergy of chemotherapeutic anticancer drugs camptothecin and doxorubicin.[44] A $NaGdF_4$ nanoprobe based on chlorides of Y^{3+}, Er^{3+}, and Tm^{3+} was coated with tantalum oxide to form lychee-shaped upconverting nanolychees (UCNL).[38] A method was reported for coating $NaGdF_4$:Yb^{3+}/Er^{3+} UCNPs with polyetheleneimine (PEI, UCNP@PEI), which enables efficient gene transfection.[39] In another example, a unique upconversion nanoparticle was developed based on Ho^{3+}, which has the potential for MR, CT, and UCL imaging. These $NaHoF_4$ (Lipo-UCNPs) nanoparticles were synthesized by thermal decomposition.[40] Another group synthesized a multifunctional $NaLuF_4$-based (Lu-UNCP) upconversion nanophosphor.[34] Rare-earth chlorides (Ln: Lu, Yb, Er/Tm) were used as core elements and proved to be stable for extended durations. Drug-carrying $BaGdF_5$-based UCNP contrast agents conjugated with Dox were found to accumulate in cancer cells preferentially, with their toxicity attributed to the change in pH after being endocytosed.[32] UCNP@SiO_2–GdDTPA nanoparticles were incubated with HeLa and L02 (immortalized hepatic) cell lines for high-contrast, live cell imaging. In-vitro CT imaging showed that UCNP@SiO_2–GdDTPA nanoparticles could enhance contrast 1.5-fold compared to the same mass concentration of Iopromide, and cells were also shown to internalize these particles.[33] When HeLa and KB cell lines were incubated with mUCNPs, in vitro results for CT gave a value of 12.45 Hounsfield units, 2.4-fold higher than Iopromide. Folic acid-conjugated mUCNPs (FA-mUCNPs) of concentration 100 μg mL^{-1} were added to HeLa, KB, and 16HBE cell lines. Almost all the cells in each case internalized FA-mUCNPs.[37]

In vitro results of CT imaging of the Lu-UCNPs suggest that they are more efficient than iodine-based contrast agents. This was attributed to the fact that the absorption of lutetium is higher than that of iodine. After carrying out stability studies for 6 months, it was concluded that Lu-UCNPs were highly stable.[34] Cytotoxicity studies for Lipo-UCNPs were carried out on BCEC and U87MG cells at concentrations as high as 800 μg mL^{-1} were found to be nontoxic. Impressive relaxometric constant ratios (r_2/r_1) of 477 and 307 were found for $NaYbF_4$ and $NaHoF_4$, respectively, which

DOI: 10.1002/smll.201500735

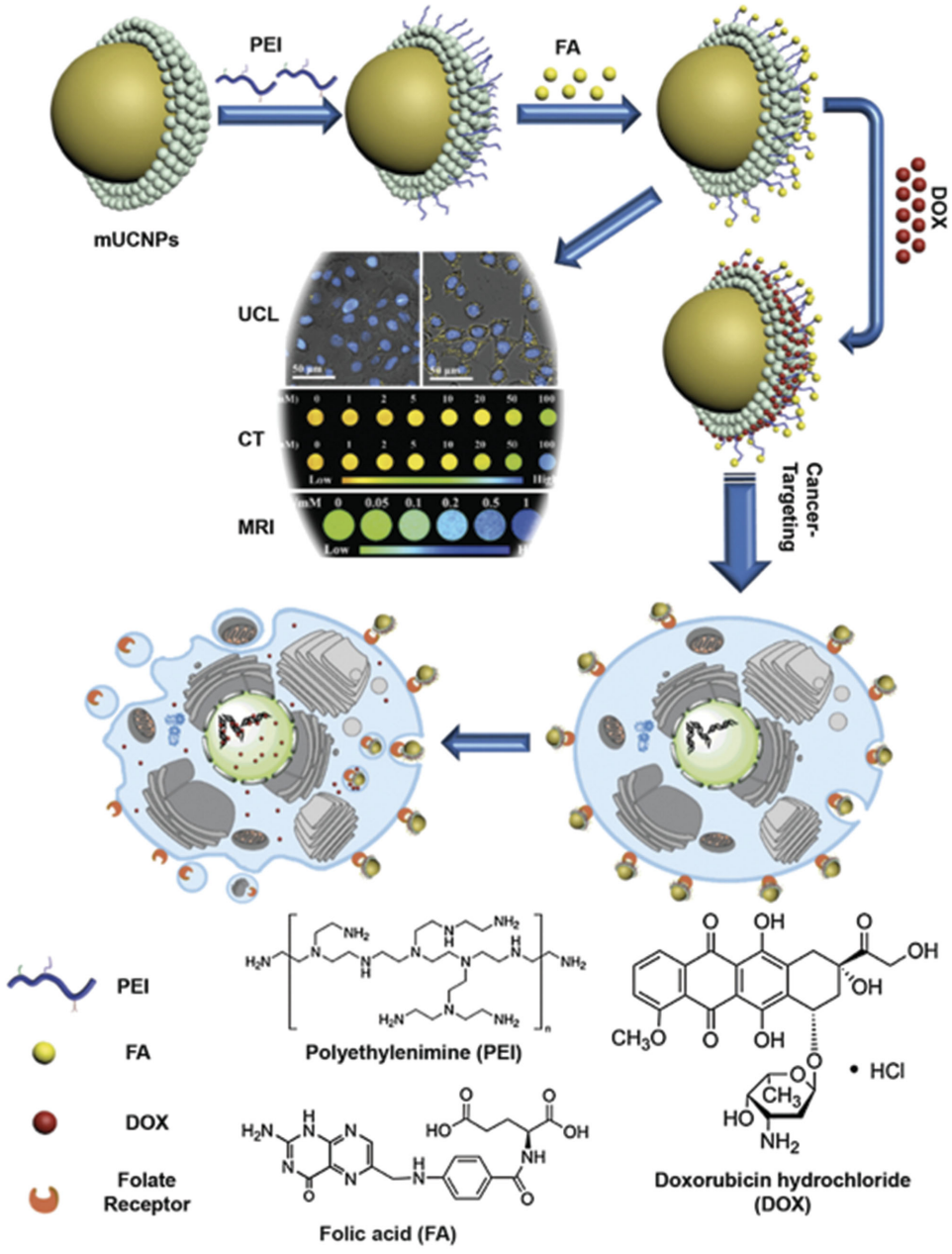

Figure 8. Structure of mesoporous core/shell UCNPs used for CT/MRI/UCL and drug loading. Schematic shows the preparation of NPs for multimodal imaging and cancer-targeting therapy. Adapted with permission.[37] Copyright 2014, Elsevier.

are higher than for commercial contrast agents like Combidex, Feridex, and Resovist. Phantom CT images for Lipo-UCNPs contained 37.2 L g^{-1}, higher than for commercial contrast agent iobitridol (15.8 Hounsfield units L g^{-1}).[40] At a concentration of 800 μg mL^{-1} of UCS-balls (100.8 μg mL^{-1} of Au), the CT clinical scanner showed a value of 250.5 HU. These results demonstrate the optimization that went into the design and synthesis of UCS-balls.[35] Trimodal CT, FL, and T1- and T2-weighted MRI images of UCNL are shown in **Figure 9**. MRI results yielded an r_1 and r_2 that were improve over previous reports. Trimodal in vitro imaging was also performed after incubation with RAW264.7 cells with UCNL (Figure 9E).[38] UCNPs@PEI was tested in vitro on HeLa and L929 cells. At a concentration of 400 μg mL^{-1}, the PEI polymer was found to be toxic compared to the same concentration of UCNP@PEI after 48 h. UCNP@PEI were internalized in HeLa cells without causing comparable cell death.[39] Likewise, $BaGdF_5$:Yb/Er UCNPs were also internalized by HeLa cells.[41]

UCNP@SiO_2–GdDTPA nanoparticles were injected intravenously in Kunming nude male mice (60 μL of 1 mg mL^{-1} NPs) and luminescence was measured. The UCL signal-to-noise ratio was 15, confirmed by ex-vivo UCL imaging. For MR imaging, 0.1 mg of the nanoparticles were injected intravenously, causing the signal from the liver to increase by 22% after 2 h.[33] For MR and CT in-vivo studies, Lu-UCNPs were injected intradermally and readings were taken 30 min later (**Figure 10**). In the case of MR imaging, there was a 54%

DOI: 10.1002/smll.201500735

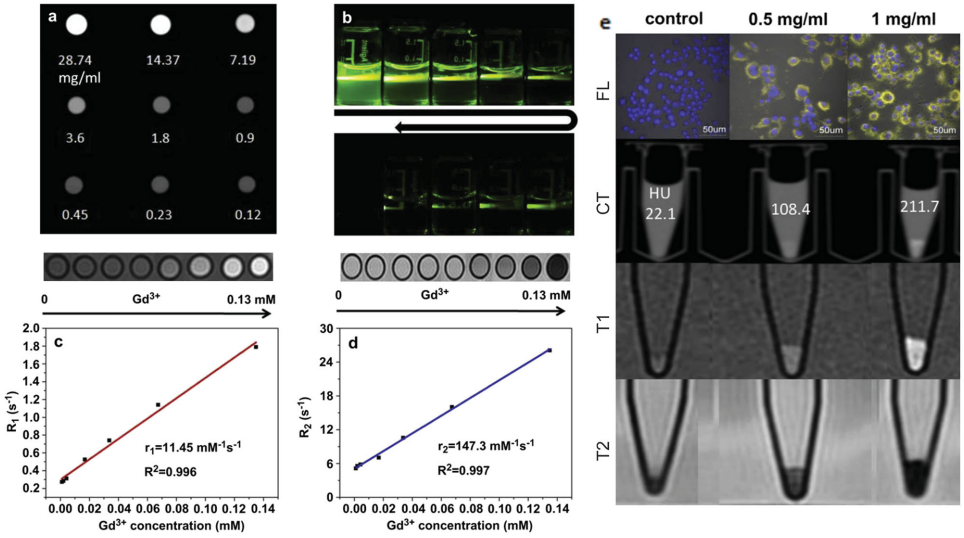

Figure 9. Trimodal imaging using upconverting nanolychees (UCNL). A) CT images and the corresponding HU values of UCNLs, B) photos of samples under 980 excitation: from 5.2 mg mL^{-1} to 0 mg mL^{-1} (water) along the direction of the arrow. C) T1-weighted MR images and relaxation rate R_1 and D) T2-weighted MR images and relaxation rate R_2. E) Trimodal imaging results in cells incubated with UCNL. From top to bottom: Fluorescence imaging, X-ray CT imaging in cell phantom (numbers indicate CT values in HU), and T1- and T2-weighted MRI. Adapted with permission.[38] Copyright 2012, Elsevier.

increase in the signal from lymph nodes 30 min post injection. CT imaging followed the same trend, showing an increase in the signal intensity with time. Also, the authors were able to pinpoint lymph nodes verified by 3D CT volume-rendered images.[34] In-vivo analyses of UCS-balls were performed on SD mice implanted with Walker 256 (tumor) cells. A 66.6% increase in signal to noise ratio post intratumoral injection was observed when ≈300 µg Gd/kg (corresponding to 1.1 mg Au kg^{-1}) was injected and imaged with MR. In CT, Hounsfield values of the tumor were found to increase from 41 to 102, whilst those values in soft tissue did not fluctuate. In case of FL imaging, the site of the tumor emitted strong visible light when irradiated with an NIR laser.[35] In MRI of UCNL, positive and negative contrast enhancement rates of T1 and T2 signal intensities were found to be increased by 5.3% and -50.2% respectively. UCL signal was detectable 30 min post tail-vein injection.[38] PAA–MUCNPs exhibited typical in-vivo nanoparticle behavior, with a slow excretion rate and accumulation in the liver and spleen. PAA–MUCNPs were intravenously injected into Kunming mice and the signals were detected in liver/spleen after 40 min and 2 h for CT and MRI, respectively. The authors also conducted an UCL study on FA–MUCNPs in nude mice bearing HeLa tumors. FA–MUCNPs were found to accumulate in the

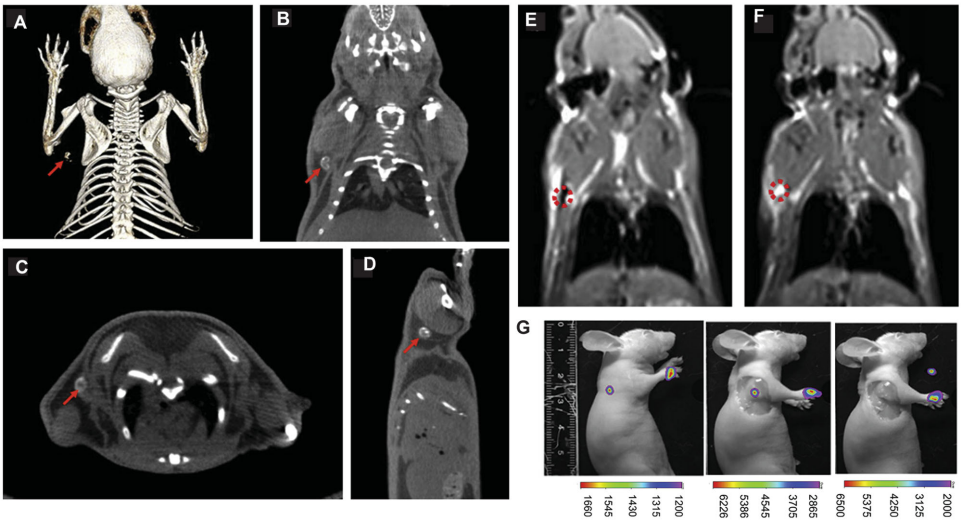

Figure 10. Trimodal CT/MR/UCL imaging using Lu-UNCPs. A) 3D CT volume-rendered and B) maximum intensity projections of coronal, C) transversal, and D) sagittal images of the lymph node obtained 30 min after intradermal injection of Lu-UCNPs. The red arrows indicate the locations of the lymph nodes. E,F) T1-weighted MR images of transversal cross-section with lymph node circled in red, before and 30 min after intradermal injection. G) In-vivo, in-situ, and ex-vivo lymphatic UCL images of nude mice lymph nodes. UCL signals were collected at 800 nm. Adapted with permission.[34] Copyright 2012, Elsevier.

DOI: 10.1002/smll.201500735

site of tumor after 3 h.[36] The efficacy of the one-pot synthesized $BaGdF_5$:Yb/Er nanoprobes as MRI and UCL imaging agents was evaluated in vivo in tumor-bearing Kunming mice. When the mice were intravenously injected with UCNPs at a 2.5 mg mL^{-1} concentration, nanoparticles accumulated in the spleen and were found to increase with time for 2 h. CT was performed after intravenous injection with 3D volume-rendered images for different time points. Based on these images, these NPs were suggested to have potential for diagnostic value in detecting splenic diseases.[41] In-vivo experiments using an intracranial glioblastoma mouse model in mice were performed using Lipo-UCNPs. Lipo-UCNPs (2%Ho with phospholipid PEGylation) were injected intravenously (240 mg kg^{-1} dose) and the T2-weighted MR signal intensity was reduced by approximately 75% in the region of brain tumor 1.5 h post injection. After successful uptake of Lipo-UCNPs in vitro, they were tested in vivo for UCL imaging. 2 h after intravenous injection of Lipo-UCNPs, there was still a sharp enhancement in UCL images.[40]

4.3. CT/MRI/US

In one validating example, CT and MRI were used to confirm the ability of US to locate therapeutic particles containing living cells administered to diabetic mice. A capsule-in-capsule (CIC) particle was developed that was capable of trimodal imaging (CT, MRI, and US) in addition to providing immunoprotection for transplanted cells.[45] The CIC structure of this particle imparts enhanced acoustic properties while the CT- and MRI-active components reaffirmed the locating ability of US. Gold nanoparticles, iron oxide nanoparticles, and Ba^{2+} were loaded on to the inner capsule made of alginate. These capsules were coated with another layer of alginate crosslinked with Ba^{2+} to produce CICs. Capsules were found to be stable for at least 3 months with no leakage of nanoparticles from the primary capsule to the secondary capsule. Female C57BL/6 mice were used, with the treatment group implanted with CICs in the peritoneal region. Spin-echo MR, gradient-echo MR, and micro-CT showed a sharp change in contrast in the regions where CICs accumulated. US imaging could locate CICs distinctly. To assess the immunoprotection aspect of CICs, CICs containing beta-TC-6 mouse insulinoma cells were transplanted into a streptozotocin-induced mouse model of type I diabetes mellitus. Blood glucose levels were found to be normal immediately after transplanting CICs and were sustained for 75 days. CICs were extracted and analyzed ex vivo by staining, which showed the transplanted cell viability to be 55%, and the capsule remained structurally intact.

4.4. MRI/PET/FL

The benefit of complimentary information that can be achieved through combined structural and molecular techniques like CT/PET or MRI/PET is well known and evidenced by the wide clinical acceptance of these multimodal scanners. Incorporation of another highly sensitive modality like FL serves to further test this technique in a preclinical context and explore the ways it might be able to complement more expensive techniques like PET, which rely on radioactive materials.

Trimodal [^{124}I]HIB-Gd-liposomes were developed from radiolabeled hexadecyl-4-iodobenzoate (HIB).[46,47] In-vitro analysis of liposomes in CT26 cells (murine colon cancer) showed that optical imaging had a higher sensitivity and better spatial resolution compared to PET. In the case of MRI, the spatial resolution was excellent but it exhibited poor sensitivity. [^{124}I]HIB-Gd-liposomes were administered to CT26 tumor-bearing BALB/c mice and some bright FL spots were apparently located in the liver. The high tissue-penetration depth of PET confirmed that the spots were originating from the liver and spleen. PET imaging also showed that the tumor was the region with second highest accumulation of liposomes after the liver, and tumor tissue was the only region that was clearly imaged with PET after 24 h. MR imaging proved to be a complementary imaging method by providing missing anatomical details, particularly with respect to soft tissues. Multiple tissues were identified, including the liver, spleen, and tumor. PET showed contrast in the bladder, although it was not detectable with FL.

Porphyrins have an excellent capacity to enhance photomedicine and diagnostics.[48–50] The potential of porphyrins as theranostic agents, when conjugated to block co-polymer–nanoporphyrins, has been demonstrated.[51] A porphyrin–telodendrimer, PEG^{5k}-Por^{4}-CA_4, was crosslinked with the help of a reversible disulphide bond to establish a more stable, crosslinked nanoporphyrin (CNP). Doxorubicin was encapsulated in the hydrophobic core with gadolinium (Gd(III)), and copper (^{64}Cu) ions were chelated in the CNPs. Photodynamic therapy (PDT) was also carried out in vitro. Glutathione level studies were conducted on PC3m (prostate cancer cell line), MB49 (mouse bladder cancer cell line), and SKOV3 (ovarian cancer cell line) cells and showed that disulphide crosslinking was reversible, based on the intracellular dissociation of CNPs. In-vivo studies were performed to evaluate the efficacy of CNPs as therapeutic (PDT and photothermal theraphy, PTT) and diagnostic (FL, MRI, PET) probes. NPs chelated with Gd(III) and ^{64}Cu proved to be excellent imaging probes, since the accumulation of these nanoparticles in the region of tumor was high.

Xie et al. developed an iron oxide nanoparticle (IONP)-based multifunctional contrast agent which has the potential to carry out PET, FL, and MR imaging.[52,53] In this work, the researchers started with coating the IONPs with dopamine. IONPs were incubated with dopamine in order to provide them with a dopamine coating and then they were coated with human serum albumin (HSA) by dispersing the dopamine-coated IONPs in HSA. To further functionalize the HSA-IONPs, DOTA and Cy5.5 were coupled to their surface. ^{64}Cu was later chelated to DOTA for PET imaging. U87MG (human glioblastoma) cells were injected subcutaneously into mice to induce tumors, and in-vitro testing was carried out with athymic nude mice bearing tumors. Phantom studies for MR imaging showed that HSA-IONP had a relaxivity (r2) of 313 mM^{-1} s^{-1}, which is higher than the commercial contrast agent Feridex. For PET/FL imaging, HSA-SPIONs

DOI: 10.1002/smll.201500735

were injected intravenously into the mice (10 mg Fe kg^{-1}). Post injection, mice were imaged and the tumor was clearly distinguishable at the 1 h time point with FL. The demarcation between tumor and normal tissue became more evident with time. Tumor-to-muscle ratio increased from 2 at the 1 h time point to 3 at the 18 h time point. PET imaging showed a similar trend to FL imaging. With ratio values of 4.5 at the 1 h time point and 8 at the 18 h time point, PET imaging yielded superior tumor-to-muscle signal ratios compared to FL. This improvement was ascribed to lesser background noise in the case of PET imaging. MR imaging studies were carried out after intravenous administration of HSA-IONPs (10 mg Fe kg^{-1}). Results post-injection in comparison with pre-injection showed a decrease of 30% in the region of the tumor after 18 h. Also, MR imaging showed that the nanoparticles were inhomogeneously distributed in the tumor. Ex-vivo results showed an accumulation of nanoparticles in the tumor and liver. Histology studies further demonstrated that the NPs accumulated in the tumor and were randomly distributed. Most of the particles were found outside vessels, suggesting extravasation to be high. However, it was realized through ex-vivo studies that there was poor correlation between nanoparticles and vasculature distribution. With Prussian blue (to visualize IONPs) and F4/80 (a macrophage marker) double staining, it was concluded that NPs in tumors were not trapped by macrophages.

Huang et al. developed a nanoprobe based on mesoporous silica which incorporates MR, PET, and optical imaging, enabling noninvasive tracking of tumor metastasis.[54] In this work, synthesis started with mixing cetyltrimethylammonium bromide (CTAB), tetraethyl orthosilicate, and fluorescent dyes (FITC/ZW800). Later, CTAB was removed to make the structures mesoporous to obtain mesoporous silica-based nanoprobes (MSNs). In the second step, Gd^{3+} ions were chelated to dye-doped MSNs through Si-Gd-DTTA to obtain dye@MSN@Gd. In the third step, MSNs were radiolabeled with ^{64}Cu to obtain dye@MSN@Gd@^{64}Cu. Gd^{3+} and ^{64}Cu were chelated to MSNs for MR and PET imaging, respectively. FITC-incorporated MSNs were used for in vitro studies and ZW800-embedded MSNs were used for in-vivo studies. For in vivo studies, mice were subcutaneously injected with 50 µL of MSNs (2 mg mL^{-1}, 20 µCi ^{64}Cu). A 4T1 tumor lymph node metastasis model was used to study the efficiency of MSNs as multimodal imaging probes in vivo. First, to study fluorescence retention in cells, FITC-MSNs were incubated with macrophages and fluorescence was visible for at least a week, showing the stability of MSNs in intracellular environments. In-vivo and ex-vivo results showed that MSNs were concentrated in tumor metastatic SLNs (T-SLN) and there was no signal was observed in normal contralateral SLNs (N-SLN). MR imaging showed that the MSNs were scattered along the margin of T-SLNs, which was in agreement with in-vivo and ex-vivo optical imaging. The MR signal was visible up to 21 days after injection in T-SLN. PET imaging showed an increase in radiotracer accumulation in T-SLNs with time, and there was no specific radiotracer signal observed in N-SLN. At the 1 h and 2 day time points T-SLN was 35- and 7-fold higher than N-SLN. Since the half-life of ^{64}Cu PET is 12.6 h it is not suited for imaging with time points over 2 days. In a clinical setup, if MSNs were to be employed, PET imaging would be carried out first followed by MR imaging. Optical imaging would be performed last since it assists in surgery.

4.5. MRI/PET/UCL

With so many combinations of NP classes, therapeutic agents, and targeting moieties being explored, finding ways to evaluate the effectiveness of each component can be challenging. Trimodal MRI, PET, and UCL can accomplish this by the MRI providing anatomical location with respect to surrounding tissues, PET can quantitatively determine the particular dose located at that region, and UCL serves as a low-background optical method to determine the local targeting efficacy. $NaGdF_4$ upconverting nanophosphors were synthesized and tagged with radiolabeled arginine-glycine-aspartic acid (RGD) in order to image the tumor angiogenesis associated with many cancers.[24,55] In-vitro incubation with U87MG was imaged with UCL and the labeled NPs were confirmed to locate on the exterior of the cell. After intravenous injection in a U87MG murine tumor model with or without blocking of the RGD targeting moiety, small animal PET and MRI were performed. PET and MRI results confirmed a contrast enhancement in the tumor location, although there was no statistical difference between models in which the target of the RGD was blocked.

4.6. MRI/PET/PA

In one example, a multimodal imaging probe using ultrasmall (<10 nm) melanin nanoparticles (MNPs).[56] The use of this pigment molecule serves to impart PA activity as well as provide an environment to facilitate the easy incorporation of PET and MRI active components. This is an attractive alternative to more complex chemical modifications that can be used to accomplish the same goal. PEG–MNPs were functionalized by conjugating RGD, then further modified with Fe^{3+} and $^{64}Cu^{2+}$. In-vitro studies were carried out with U87MG cells and in-vivo studies were done on female athymic nude mice bearing tumors derived from the same cells. For MRI, in-vitro results showed that the nanoparticles carried a relaxivity (r1) value of 1.2 mM^{-1} s^{-1}. Cellular uptake of ^{64}Cu-labeled PEG-MNPs doubled after conjugating these nanoparticles to RGD peptide. For MRI, mice were imaged 4 h after injection and showed a 30% increase in signal intensity in the region of the tumor. In-vivo results for PET imaging showed that the uptake of RGD nanoparticles increased in the region of the tumor to 6% injected dose per gram of tissue after 24 h. The nanoparticles that passed were cleared through the hepatobiliary system.

4.7. MRI/PET/Cerenkov

Because the applications and benefits of Cerenkov imaging are still actively being investigated, the ability to compare it directly with modalities like MRI and PET is useful. With a

DOI: 10.1002/smll.201500735

single trimodal probe active in each modality, it is possible to obtain effective comparisons. ^{124}I-labeled thermally cross-linked SPIONs (TCL-SPIONs) were used to identify and image the sentinel lymph node (SLN) in mice. These particles did not exhibit any aggregation and were stable for up to half a year. Their T2 values were also higher than Feridex. The two front paws of BALB/c mice were injected with the ^{124}I-labeled TCL-SPIONs after the mouse breast cancer cell line 4T1 was introduced into the left shoulder ten days prior. MRI, PET, and Cerenkov imaging were then performed to determine if the lymph node close to the injected cancer cells could be differentiated from the SLNs not located close. An indication of reduced uptake in the SLN closest to the cancer cells was noticed in all three imaging modalities consistently.[57] When ^{68}Ga-SPIONs were also used to visualize SLN in these modalities, PET, MR, and Cerenkov imaging were able to clearly locate the nodes. An inhomogeneity of the SLN ^{68}Ga-SPIONs signal in metastatic SLNs was also observed.[58,59]

4.8. MRI/SPECT/FL

As multimodal MR scanners start to enter the market, it will be important to emphasize their versatility in imaging paradigms. Being able to design multimodal probes for MRI and SPECT may enhance the utility of these scanners. At least two trimodal MRI/SPECT/FL contrast agents have been developed; a functionalized polymeric imaging agent based on high-molecular-weight poylglycerol (HPG) with DOTA (HPGD),[60] and SPIONs labeled with ^{99m}Tc and Alexa dye to form ^{99m}Tc-AF-SPIONs.[61] HPG was functionalized with Gd^{3+}, ^{111}In, and Alexa dye. Human vascular endothelial cells (HUVECs) were found to exhibit almost 100% viability when incubated with HPG and HPGD at the same concentration. Relaxivity (r_1) of HPGD-Gd was found to be significantly higher than for commercial agents like Galbumin. Subcutaneous injection of 99mTc-AF-SPIONs in the hind paw of Wistar rats resulted in clear visualization of SLNs in MRI, SPECT, and FL after 5 h. HPGD-Gd were alternatively injected intravenously into female C57Bl/6 mice and accumulation in the region of tumor was found to be maximal 3 days post-injection. The biodistribution of ^{111}In-HPGD showed considerable increase in the accumulation of NPs in the tumor region with a peak value on day three. PET and MRI were helpful for visualizing the target in whole body scans during lymph node imaging of ^{99m}Tc-AF-SPIONs, after which FL could be used intraoperatively to highlight the target. The ability to perform this imaging during surgery then quantify the target ex vivo with either optical or radiologic techniques highlights the synergistic effects of multimodal imaging.

4.9. MRI/US/PA

US and PA, which both rely on ultrasonic detection, are naturally amenable to simultaneous detection with respect to instrumentation implementation. Microcapsules were synthesized with poly(lactic acid) loaded with IO nanoparticles (IO@PLA/GO).[62] MRI of nude mice after intratumorally injection with a 20 mg kg^{-1} dose showed considerable enhancement in local contrast. Pulse-inversed harmonic imaging (US) carried out on New Zealand white rabbits showed that the contrast enhancement persisted for 5 min, in accordance with clinical expectations. NPs placed under 44 mm of chicken breast were still detectable with PA at a concentration of 32 mg mL^{-1}. PTT applications were confirmed in vitro, showing the NPs to have a therapeutic character when irradiated.

4.10. MRI/PA/Raman

The many levels of complexity in organs and tissues can make the systemic evaluation of disease and treatment challenging. When trying to analyze a complicated disease and procedure such as brain tumor surgery, multiple procedures are needed to determine the anatomical, physiological, and cellular status at the location of interest. Reducing the time, risk, and cost to patients in this situation has been addressed with trimodal MRI, PA, and Raman imaging. This imaging agent (MPR nanoparticles) is synthesized from a 60 nm Au core coated with a Raman-active molecular trans-1,2-bis(4-pyridyl)-ethylene, given a protective coating of silica, and enriched with malemide-DOTA-Gd.[4] MPRs were subcutaneously injected into nude mice, followed by MRI, PA, and Raman signal evaluations. Signal intensity was found to be highly correlated to the concentration and Raman imaging was the most sensitive imaging method, followed by photoacoustic and MR imaging. For in-vivo experiments, mice with orthotopic brain tumors were injected with MPRs intravenously. In-vivo MRI and PA of mice implanted with $eGFP^+$U87MG exhibited signal enhancements 30 min post injection. The MRI signal was monitored until 24 h and there was no decrease in the signal intensity compared to the 2 h reading, whereas Gd-based imaging agents are flushed out in few minutes. In the case of Raman imaging, there was peak as soon as MPRs were injected but that was attributed to the nonspecific circulation of MPRs in superficial layers. Distribution of MPRs was validated by histology. MPRs were found only in the region of the tumor and tumor boundaries, and none were seen in the surrounding healthy tissue. The potential of MPRs for PA and Raman imaging in guided tumor re-section was examined via the craniotomy of mice with visible tumors re-sected. High-resolution Raman images were obtained before and after resection, and finger-like projections were observed around the re-sected area where MPRs were found to be concentrated. More histological investigation of these areas led to the conclusion that they were minute projections of tumor. This example illustrates the potential benefit that higher-order multimodal probes offer.

4.11. US/PA/FL

In order to accomplish trimodal US, PA, and FL imaging, a porphyrin-lipid based microbubble[63–65] composed of a

DOI: 10.1002/smll.201500735

porphyrin-lipid together with conventional lipids was formed that encapsulated perfluoropropane gas. The porphyrin-lipid was previously used to develop liposome-like nanovesicles and has excellent potential for multimodal targeted approaches.[66–69] Compared to unimodal microbubbles made from traditional phospholipids, there was no change observed with respect to US, however, PA was enhanced 40-fold, and FL 17-fold.[64] Porphyrin-lipid microbubbles were injected into KB tumor-bearing-xenograft mice intravenously. The contrast of the US images in the case of conventional and porphyrin-lipid microbubbles was enhanced in a similar fashion. An increase in PA signal intensity was evident only for the porphyrin-lipid microbubbles. Porphyrin-lipid microbubbles enhanced signals in the tumor compared to healthy tissue, illustrating the potential for ex-vivo imaging either as a source for verifying drug accumulation or to estimate biodistribution.

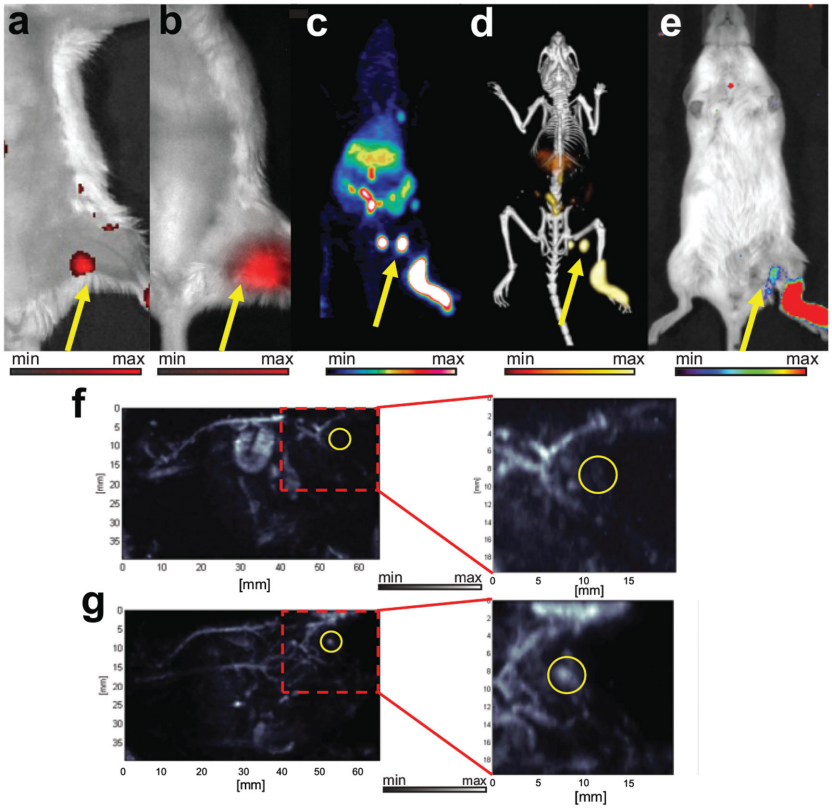

Figure 11. Hexamodal lymphatic imaging using PoP-UCNPs in mice. PoP-UCNPs were injected in the rear left footpad and imaged in six modalities 1 hpost-injection. Accumulation of PoP-UCNPs in the first draining lymph node is indicated with yellow arrows. a) FL and b) UC images with the injection site cropped out of frame. c) Full anatomy PET, d) merged PET/CT, and e) Cerenkov images. f) PA images before and g) after injection show an endogenous PA blood signal compared to the contrast enhancement for visualization of the previously undetected lymph node. Adapted with permission.[76] Copyright 2015, Wiley.

4.12. PET/FL/UCL

FL and UCL both involve photon absorption and emission processes and are similar in implementation. In theory, the two types of imaging could provide complementary information, with UCL being better suited for deeper imaging. Because the combinations of materials, synthetic procedures, and applications of nanoparticles in imaging are virtually endless, it is important to find ways of characterizing these novel agents. Trimodal PET, FL, and UCL imaging was used to validate a range of nanoparticle synthetic techniques and applications.[70] Alpha-cyclodextrin was used as the host material and could solubilize particles regardless of size or synthesis method (thermal decomposition, hydrothermal, solvothermal). Besides the physical characterizations, trimodal imaging was carried out in cell labeling and in-vivo lymphatic imaging.

4.13. Bioluminescence

Bioluminescence, which involves the enzymatic activation of light-generating chemicals, is not considered an exogenous contrast mode, but rather is used to unambiguously identify genetically modified cells (such as cancer cells) in vivo. Nevertheless, there are some multimodal examples involving bioluminescence worth noting. When other modalities such as PET and CT are combined with bioluminescence, co-localization of the contrast agent with the tumor can be assessed. A trimodal imaging probe was developed to detect cancerous xenografts from different cell lines and whether a melanoma cell line had metastasized in a murine model.[71] CT and PET both registered the xenografts at the same location and combined PET/CT showed lesions that were not visible in CT alone. All three modalities registered the signals of melanoma metastases, which was confirmed with ex-vivo assays. A PET, FL, and bioluminescent reporter gene was also developed for whole-body imaging.[72] Whole-body imaging was performed after administration of D-luciferin to generate the bioluminescent signal and was successful in all three modalities.

4.14. Higher-Order Multimodality

The examples described above refer to trimodal imaging agents. To date, there have also been recent examples of imaging agents that demonstrate contrast in four, five, or six modalities. These hypermodal agents at this stage are more conceptual than practical, but in theory one day could simplify and streamline medical imaging. Additionally, since techniques such as MRI and CT sometimes must be avoided by patients with the presence of a metal implant or with risk of overexposure to radiation, a universal imaging agent could provide invaluable versatility.

DOI: 10.1002/smll.201500735

$NaLuF_4$-based optimized nanoparticles with the potential for tetramodal imaging (MR, CT, SPECT, and UCL imaging) were recently developed.[35,73] In-vitro studies were carried out on macrophages and in-vivo studies on nude mice with or without KB tumors. From the phantom studies carried out with $NaLuF_4$:Yb^{3+}, Tm^{3+}@$NaGdF_4$-(^{153}Sm) NPs for CT imaging, it was concluded that these nanoparticles at 1 mg mL^{-1} concentration show the same X-ray attenuation as 1.6 mg mL^{-1} of Iopromide. The signal-to-noise ratio for UCL imaging in vivo was found to be 21. For in-vivo studies, mice were injected with 800 µL of $NaLuF_4$:Yb^{3+}, Tm^{3+}@$NaGdF_4$-(^{153}Sm) nanoparticles (30 mg mL^{-1}) and, 1 h later, high X-ray attenuation was observed in the regions of the liver and spleen. Nude mice bearing KB tumors were used to probe for tumor angiogenesis. CT showed high attenuation in the region of the tumor, MR detected an intense signal from the surface of the tumor, SPECT imaging showed a strong signal in the region of the tumor and also assisted in the quantification (1.7% of the total dose was within the tumor), and UCL imaging aided in an histochemical analysis of tumor angiogenesis. These results demonstrate the potential benefits of multimodal imaging probes and highlight the synergistic value of multimodal imaging data.

A magnetic–fluorescent–bioluminescent–radioisotopic particle (MFBR) was synthesized for quadruple modality MRI, PET, FL, bioluminescence.[74] These particles were incorporated into the rat glioma cell line C6 before being injected at different tissue depths in normal nude mice. Bioluminescence was detected at both intramuscular and subcutaneous locations, which was further validated by µPET. These NPs demonstrated the capacity of multimodal nanoprobes to be used for stem-cell tracking at different levels in the body via four combined imaging modalities.

Nanoparticulate platforms for pentamodal[75] and hexamodal[76] imaging have also been developed for proof-of-principle studies in recent years. Rieffel et al. utilized a UCNP core, porphyrin-phospholipid (PoP), and post-synthesis chelation of a PET radiotracer to render these NPs (PoP-UCNPs) suitable for multimodal in-vivo diagnostics.[76] The signal penetration and resolution for each modality was tested as a function of tissue depth, with CT and PET imaging performing best in both categories. In vivo, the PoP-UCNPs were administered to the rear footpad of BALB/c mice and imaged in each modality. The first lymph node draining the injection site was detected in PET, FL, UCL, PA, and Cerenkov imaging (**Figure 11**) with CT capabilities confirmed in phantom samples. This NP shows how a relatively simple agent can be used for a wide range of imaging modalities.

5. Conclusion

While advances in clinical and preclinical imaging modalities will continue to push the limits of what can be accomplished, higher-order multimodal imaging holds the potential to unite or bridge different imaging modalities. Nanoparticulate approaches are most likely required to make better use of complimentary imaging technologies to reinforce a cycle of progress. Not only have some multimodal probes shown to be competitive with existing clinical imaging agents, many also hold a therapeutic capacity.[77] Many of the multimodal contrast agents developed so far incorporate an MR-active component, which reflects the clinical importance of MRI. The next steps in translating these multimodal probes from the bench to the clinic include more detailed and rigorous investigations of their in-vivo pharmacokinetic and toxicity profiles. Additionally, large-scale manufacturing protocols should be established that characterize the colloidal, chemical, and storage stability of the NPs. Crucially, synergistic imaging applications that address unmet needs must be identified. Although the versatility of nanoprobes in medicine and imaging has been one of the biggest stimuli towards multimodality, simplification is also a viable strategy towards clinical implementation. In experimental design, this may mean sacrificing novel targeting ligands or therapeutics in favor of less complex probes based on materials that can be, or that already are, clinically approved. Higher-order multimodal probes hold great research potential and, with motivated efforts, may eventually shift biomedical imaging paradigms.

Acknowledgements

This work was supported by the National Institutes of Health (1R01CA169365 and DP5OD017898).

[1] N. Beckmann, *Brazilian J. Phys.* **2006**, *36*, 16–22.
[2] J. K. Willmann, N. van Bruggen, L. M. Dinkelborg, S. S. Gambhir, *Nat. Rev. Drug Discov.* **2008**, *7*, 591–607.
[3] M. L. James, S. S. Gambhir, *Physiol. Rev.* **2012**, *92*, 897–965.
[4] M. F. Kircher, A. de la Zerda, J. V. Jokerst, C. L. Zavaleta, P. J. Kempen, E. Mittra, K. Pitter, R. Huang, C. Campos, F. Habte, R. Sinclair, C. W. Brennan, I. K. Mellinghoff, E. C. Holland, S. S. Gambhir, *Nat. Med.* **2012**, *18*, 829–834.
[5] J. Kim, Y. Piao, T. Hyeon, *Chem. Soc. Rev.* **2009**, *38*, 372–390.
[6] A. Louie, *Chem. Rev.* **2010**, *110*, 3146–3195.
[7] J. Cheon, J.-H. Lee, *Acc. Chem. Res.* **2008**, *41*, 1630–1640.
[8] W. J. M. Mulder, G. J. Strijkers, G. A. F. van Tilborg, D. P. Cormode, Z. A. Fayad, K. Nicolay, *Acc. Chem. Res.* **2009**, *42*, 904–914.
[9] D.-E. Lee, H. Koo, I.-C. Sun, J. H. Ryu, K. Kim, I. C. Kwon, *Chem. Soc. Rev.* **2012**, *41*, 2656–2672.
[10] F. A. Mettler, W. Huda, T. T. Yoshizumi, M. Mahesh, *Radiology* **2008**, *248*, 254–263.
[11] R. Smith-Bindman, J. Lipson, R. Marcus, K. P. Kim, M. Mahesh, R. Gould, A. Berrington de González, D. L. Miglioretti, *Arch. Intern. Med.* **2009**, *169*, 2078–2086.
[12] H. G. Potter, B. J. Nestor, C. M. Sofka, S. T. Ho, L. E. Peters, E. A. Salvati, *J. Bone Joint Surg. Am.* **2004**, *86-a*, 1947–54.
[13] E. Bombardieri, C. Aktolun, R. Baum, A. Bishof-Delaloye, J. Buscombe, J. Chatal, L. Maffioli, R. Moncayo, L. Mortelmans, S. Reske, *Eur. J. Nucl. Med. Mol. Imaging* **2003**, *30*, B115–B124.
[14] H. Zhu, S. O. Isikman, O. Mudanyali, A. Greenbaum, A. Ozcan, *Lab Chip* **2013**, *13*, 51–67.
[15] Y. Pan, J.-P. Volkmer, K. E. Mach, R. V. Rouse, J.-J. Liu, D. Sahoo, T. C. Chang, T. J. Metzner, L. Kang, M. van de Rijn, E. C. Skinner, S. S. Gambhir, I. L. Weissman, J. C. Liao, *Sci. Transl. Med.* **2014**, *6*, 260ra148.
[16] L. V. Wang, L. Gao, *Annu. Rev. Biomed. Eng.* **2014**, *16*, 155–185.

DOI: 10.1002/smll.201500735

[17] C. L. Zavaleta, B. R. Smith, I. Walton, W. Doering, G. Davis, B. Shojaei, M. J. Natan, S. S. Gambhir, *Proc. Natl. Acad. Sci. USA* **2009**, *106*, 13511–13516.
[18] B. G. Wilson, *Radiologic Technol.* **2005**, *76*, 301–13; quiz 314–6, 319.
[19] H. U. Gerth, K. U. Juergens, U. Dirksen, J. Gerss, O. Schober, C. Franzius, *J. Nucl. Med.* **2007**, *48*, 1932–1939.
[20] F. Wang, D. Banerjee, Y. Liu, X. Chen, X. Liu, *Analyst* **2010**, *135*, 1839–1854.
[21] L. Cheng, K. Yang, Y. Li, J. Chen, C. Wang, M. Shao, S.-T. Lee, Z. Liu, *Angew. Chem. Int. Ed.* **2011**, *123*, 7523–7528.
[22] R. Koole, W. J. M. Mulder, M. M. van Schooneveld, G. J. Strijkers, A. Meijerink, K. Nicolay, *WIRES: Nanomed. Nanobiotechnol.* **2009**, *1*, 475–491.
[23] J. R. McCarthy, R. Weissleder, *Adv. Drug Deliv. Rev.* **2008**, *60*, 1241–1251.
[24] W. J. Rieter, J. S. Kim, K. M. L. Taylor, H. An, W. Lin, T. Tarrant, W. Lin, *Angew. Chem. Int. Ed.* **2007**, *46*, 3680–3682.
[25] N. Mitchell, T. L. Kalber, M. S. Cooper, K. Sunassee, S. L. Chalker, K. P. Shaw, K. L. Ordidge, A. Badar, S. M. Janes, P. J. Blower, M. F. Lythgoe, H. C. Hailes, A. B. Tabor, *Biomaterials* **2013**, *34*, 1179–1192.
[26] D. P. Cormode, T. Skajaa, M. M. van Schooneveld, R. Koole, P. Jarzyna, M. E. Lobatto, C. Calcagno, A. Barazza, R. E. Gordon, P. Zanzonico, E. A. Fisher, Z. A. Fayad, W. J. M. Mulder, *Nano Lett.* **2008**, *8*, 3715–3723.
[27] M. M. van Schooneveld, D. P. Cormode, R. Koole, J. T. van Wijngaarden, C. Calcagno, T. Skajaa, J. Hilhorst, D. C. t. Hart, Z. A. Fayad, W. J. M. Mulder, A. Meijerink, *Contrast Media Mol. Imaging* **2010**, *5*, 231–236.
[28] W. Dong, Y. Li, D. Niu, Z. Ma, X. Liu, J. Gu, W. Zhao, Y. Zheng, J. Shi, *Small* **2013**, *9*, 2500–2508.
[29] W. Dong, Y. Li, D. Niu, Z. Ma, J. Gu, Y. Chen, W. Zhao, X. Liu, C. Liu, J. Shi, *Adv. Mater.* **2011**, *23*, 5392–5397.
[30] J. Zhou, Z. Lu, G. Shan, S. Wang, Y. Liao, *Biomaterials* **2014**, *35*, 368–377.
[31] S. Xue, Y. Wang, M. Wang, L. Zhang, X. Du, H. Gu, C. Zhang, *Int. J. Nanomedicine* **2014**, *9*, 2527–2538.
[32] D. Yang, Y. Dai, J. Liu, Y. Zhou, Y. Chen, C. Li, P. a. Ma, J. Lin, *Biomaterials* **2014**, *35*, 2011–2023.
[33] A. Xia, M. Chen, Y. Gao, D. Wu, W. Feng, F. Li, *Biomaterials* **2012**, *33*, 5394–5405.
[34] J. Zhou, X. Zhu, M. Chen, Y. Sun, F. Li, *Biomaterials* **2012**, *33*, 6201–6210.
[35] H. Xing, W. Bu, S. Zhang, X. Zheng, M. Li, F. Chen, Q. He, L. Zhou, W. Peng, Y. Hua, J. Shi, *Biomaterials* **2012**, *33*, 1079–1089.
[36] J.-W. Shen, C.-X. Yang, L.-X. Dong, H.-R. Sun, K. Gao, X.-P. Yan, *Anal. Chem.* **2013**, *85*, 12166–12172.
[37] L. Zhou, X. Zheng, Z. Gu, W. Yin, X. Zhang, L. Ruan, Y. Yang, Z. Hu, Y. Zhao, *Biomaterials* **2014**, *35*, 7666–7678.
[38] Q. Xiao, W. Bu, Q. Ren, S. Zhang, H. Xing, F. Chen, M. Li, X. Zheng, Y. Hua, L. Zhou, W. Peng, H. Qu, Z. Wang, K. Zhao, J. Shi, *Biomaterials* **2012**, *33*, 7530–7539.
[39] L. Wang, J. Liu, Y. Dai, Q. Yang, Y. Zhang, P. Yang, Z. Cheng, H. Lian, C. Li, Z. Hou, P. a. Ma, J. Lin, *Langmuir* **2014**, *30*, 13042–13051.
[40] D. Ni, W. Bu, S. Zhang, X. Zheng, M. Li, H. Xing, Q. Xiao, Y. Liu, Y. Hua, L. Zhou, W. Peng, K. Zhao, J. Shi, *Adv. Funct. Mater.* **2014**, *24*, 6613–6620.
[41] S. Zeng, M.-K. Tsang, C.-F. Chan, K.-L. Wong, J. Hao, *Biomaterials* **2012**, *33*, 9232–9238.
[42] A. Xia, Y. Gao, J. Zhou, C. Li, T. Yang, D. Wu, L. Wu, F. Li, *Biomaterials* **2011**, *32*, 7200–7208.
[43] C. Liu, Z. Gao, J. Zeng, Y. Hou, F. Fang, Y. Li, R. Qiao, L. Shen, H. Lei, W. Yang, M. Gao, *ACS Nano* **2013**, *7*, 7227–7240.
[44] G. Tian, W. Yin, J. Jin, X. Zhang, G. Xing, S. Li, Z. Gu, Y. Zhao, *J. Mater. Chem. B* **2014**, *2*, 1379–1389.
[45] J. Kim, D. R. Arifin, N. Muja, T. Kim, A. A. Gilad, H. Kim, A. Arepally, T. Hyeon, J. W. M. Bulte, *Angew. Chem. Int. Ed.* **2011**, *123*, 2365–2369.
[46] J. Kim, D. N. Pandya, W. Lee, J. W. Park, Y. J. Kim, W. Kwak, Y. S. Ha, Y. Chang, G. I. An, J. Yoo, *ACS Med. Chem. Lett.* **2014**, *5*, 390–394.
[47] J. C. Park, G. I. An, S. I. Park, J. Oh, H. J. Kim, Y. S. Ha, E. K. Wang, K. M. Kim, J. Y. Kim, J. Lee, M. J. Welch, J. Yoo, *Nucl. Med. Biol.* **2011**, *38*, 321–9.
[48] Y. Zhang, J. F. Lovell, *Theranostics* **2012**, *2*, 905–15.
[49] H. Huang, W. Song, J. Rieffel, J. F. Lovell, *Frontiers Phys.* **2015**, 3.
[50] J. F. Lovell, T. W. B. Liu, J. Chen, G. Zheng, *Chem. Rev.* **2010**, *110*, 2839–2857.
[51] Y. Li, T.-y. Lin, Y. Luo, Q. Liu, W. Xiao, W. Guo, D. Lac, H. Zhang, C. Feng, S. Wachsmann-Hogiu, J. H. Walton, S. R. Cherry, D. J. Rowland, D. Kukis, C. Pan, K. S. Lam, *Nat. Commun.* **2014**, DOI: 10.1038/ncomms5712.
[52] J.-s. Choi, J. C. Park, H. Nah, S. Woo, J. Oh, K. M. Kim, G. J. Cheon, Y. Chang, J. Yoo, J. Cheon, *Angew. Chem. Int. Ed.* **2008**, *47*, 6259–6262.
[53] J. Xie, K. Chen, J. Huang, S. Lee, J. Wang, J. Gao, X. Li, X. Chen, *Biomaterials* **2010**, *31*, 3016–3022.
[54] X. Huang, F. Zhang, S. Lee, M. Swierczewska, D. O. Kiesewetter, L. Lang, G. Zhang, L. Zhu, H. Gao, H. S. Choi, G. Niu, X. Chen, *Biomaterials* **2012**, *33*, 4370–4378.
[55] L. Junghan, L. Tae Sup, R. Jiyoung, H. Sukmin, K. Moonsik, I. Kangbin, K. Joo Hyun, L. Sang Moo, P. Sun, S. Rita, *J. Nucl. Med.* **2013**, *54*, 96–103.
[56] Q. Fan, K. Cheng, X. Hu, X. Ma, R. Zhang, M. Yang, X. Lu, L. Xing, W. Huang, S. S. Gambhir, Z. Cheng, *J. Am. Chem. Soc.* **2014**, *136*, 15185–15194.
[57] J. C. Park, M. K. Yu, G. I. An, S.-I. Park, J. Oh, H. J. Kim, J.-H. Kim, E. K. Wang, I.-H. Hong, Y. S. Ha, T. H. Choi, K.-S. Jeong, Y. Chang, M. J. Welch, S. Jon, J. Yoo, *Small* **2010**, *6*, 2863–2868.
[58] R. Madru, P. Kjellman, F. Olsson, K. Wingårdh, C. Ingvar, F. Ståhlberg, J. Olsrud, J. Lätt, S. Fredriksson, L. Knutsson, S.-E. Strand, *J. Nucl. Med.* **2012**, *53*, 459–463.
[59] R. Madru, T. A. Tran, J. Axelsson, C. Ingvar, A. Bibic, F. Ståhlberg, L. Knutsson, S.-E. Strand, *Am. J. Nucl. Med. Mol. Imaging* **2014**, *4*, 60–69.
[60] K. Saatchi, P. Soema, N. Gelder, R. Misri, K. McPhee, J. H. E. Baker, S. A. Reinsberg, D. E. Brooks, U. O. Häfeli, *Bioconjugate Chem.* **2012**, *23*, 372–381.
[61] R. Madru, P. Svenmarker, C. Ingvar, F. Ståhlberg, S.-A. Engels, L. Knutsson, S.-E. Strand, *Diagnostics* **2014**, *4*, 13–26.
[62] X.-D. Li, X.-L. Liang, X.-L. Yue, J.-R. Wang, C.-H. Li, Z.-J. Deng, L.-J. Jing, L. Lin, E.-Z. Qu, S.-M. Wang, C.-L. Wu, H.-X. Wu, Z.-F. Dai, *J. Mater. Chem. B* **2014**, *2*, 217–223.
[63] E. Huynh, J. F. Lovell, B. L. Helfield, M. Jeon, C. Kim, D. E. Goertz, B. C. Wilson, G. Zheng, *J. Am. Chem. Soc.* **2012**, *134*, 16464–16467.
[64] E. Huynh, C. S. Jin, B. C. Wilson, G. Zheng, *Bioconjugate Chem.* **2014**, *25*, 796–801.
[65] E. Huynh, B. Y. Leung, B. L. Helfield, M. Shakiba, J. A. Gandier, C. S. Jin, E. R. Master, B. C. Wilson, D. E. Goertz, G. Zheng, *Nat. Nanotechnol.* **2015**, *10*, 325–32.
[66] J. F. Lovell, C. S. Jin, E. Huynh, H. Jin, C. Kim, J. L. Rubinstein, W. C. W. Chan, W. Cao, L. V. Wang, G. Zheng, *Nat. Mater.* **2011**, *10*, 324–332.
[67] J. F. Lovell, C. S. Jin, E. Huynh, T. D. MacDonald, W. Cao, G. Zheng, *Angew. Chem. Int. Ed.* **2012**, *51*, 2429–2433.
[68] K. A. Carter, S. Shao, M. I. Hoopes, D. Luo, B. Ahsan, V. M. Grigoryants, W. Song, H. Huang, G. Zhang, R. K. Pandey, J. Geng, B. A. Pfeifer, C. P. Scholes, J. Ortega, M. Karttunen, J. F. Lovell, *Nat. Commun.* **2014**, DOI: 10.1038/ncomms4546.

[69] S. Shao, J. Geng, H. Ah Yi, S. Gogia, S. Neelamegham, A. Jacobs, J. F. Lovell, *Nat. Chem.* **2015**, *7*, 438–446.
[70] Q. Liu, M. Chen, Y. Sun, G. Chen, T. Yang, Y. Gao, X. Zhang, F. Li, *Biomaterials* **2011**, *32*, 8243–8253.
[71] C. M. Deroose, A. De, A. M. Loening, P. L. Chow, P. Ray, A. F. Chatziioannou, S. S. Gambhir, *J. Nucl. Med.* **2007**, *48*, 295–303.
[72] V. Ponomarev, M. Doubrovin, I. Serganova, J. Vider, A. Shavrin, T. Beresten, A. Ivanova, L. Ageyeva, V. Tourkova, J. Balatoni, W. Bornmann, R. Blasberg, J. Gelovani Tjuvajev, *Eur. J. Nucl. Med. Mol. Imaging* **2004**, *31*, 740–751.
[73] Y. Sun, X. Zhu, J. Peng, F. Li, *ACS Nano* **2013**, *7*, 11290–11300.
[74] H. Do Won, K. Hae Young, K. Suk-Ki, K. Daehong, L. Dong Soo, K. Soonhag, *Chem. Eur. J.* **2009**, *15*, 9387–9393.
[75] Y. Liu, Z. Chang, H. Yuan, A. M. Fales, T. Vo-Dinh, *Nanoscale* **2013**, *5*, 12126–12131.
[76] J. Rieffel, F. Chen, J. Kim, G. Chen, W. Shao, S. Shao, U. Chitgupi, R. Hernandez, S. A. Graves, R. J. Nickles, P. N. Prasad, C. Kim, W. Cai, J. F. Lovell, *Adv. Mater.* **2015**, *27*, 1785–1790.
[77] D. Luo, K. A. Carter, J. F. Lovell, *WIRES: Nanomed. Nanobiotechnol.* **2015**, *7*, 169–188.
[78] A. Drzezga, M. Souvatzoglou, M. Eiber, A. J. Beer, S. Fürst, A. Martinez-Möller, S. G. Nekolla, S. Ziegler, C. Ganter, E. J. Rummeny, M. Schwaiger, *J. Nucl. Med.* **2012**, *53*, 845–855.

Received: March 16, 2015
Revised: April 27, 2015
Published online: